One-dimensional van der Waals heterostructures: Growth mechanism and handedness correlation revealed by nondestructive TEM

Yongjia Zheng[a,1], Akihito Kumamoto[b,1], Kaoru Hisama[a], Keigo Otsuka[a], Grace Wickerson[c,2], Yuta Sato[d], Ming Liu[a], Taiki Inoue[e], Shohei Chiashi[a], Dai-Ming Tang[f], Qiang Zhang[g], Anton Anisimov[h], Esko I. Kauppinen[g], Yan Li[i], Kazu Suenaga[d,j], Yuichi Ikuhara[b], Shigeo Maruyama[a,3], and Rong Xiang[a,3]

[a]Department of Mechanical Engineering, The University of Tokyo, Tokyo 113-8656, Japan; [b]Institute of Engineering Innovation, The University of Tokyo, Tokyo 113-8656, Japan; [c]Department of Materials Science and Nanoengineering, Rice University, Houston, TX 77005; [d]Nanomaterials Research Institute, National Institute of Advanced Industrial Science and Technology, Tsukuba 305-8565, Japan; [e]Department of Applied Physics, Osaka University, Osaka 565-0871, Japan; [f]World Premier International Center for Materials Nanoarchitectonics, National Institute for Materials Science, Tsukuba 3050044, Japan; [g]Department of Applied Physics, Aalto University School of Science, FI-00076 Aalto, Finland; [h]Canatu Ltd., SF-01720 Vantaa, Finland; [i]College of Chemistry and Molecular Engineering, Peking University, Beijing 100871, China; and [j]The Institute of Scientific and Industrial Research, Osaka University, Osaka 567-0047, Japan

Edited by Phaedon Avouris, IBM Thomas J. Watson Research Center, Brooklyn, NY, and approved August 6, 2021 (received for review April 17, 2021)

We recently synthesized one-dimensional (1D) van der Waals heterostructures in which different atomic layers (e.g., boron nitride or molybdenum disulfide) seamlessly wrap around a single-walled carbon nanotube (SWCNT) and form a coaxial, crystalized heteronanotube. The growth process of 1D heterostructure is unconventional—different crystals need to nucleate on a highly curved surface and extend nanotubes shell by shell—so understanding the formation mechanism is of fundamental research interest. In this work, we perform a follow-up and comprehensive study on the structural details and formation mechanism of chemical vapor deposition (CVD)–synthesized 1D heterostructures. Edge structures, nucleation sites, and crystal epitaxial relationships are clearly revealed using transmission electron microscopy (TEM). This is achieved by the direct synthesis of heteronanotubes on a CVD-compatible Si/SiO_2 TEM grid, which enabled a transfer-free and nondestructive access to many intrinsic structural details. In particular, we have distinguished different-shaped boron nitride nanotube (BNNT) edges, which are confirmed by electron diffraction at the same location to be strictly associated with its own chiral angle and polarity. We also demonstrate the importance of surface cleanness and isolation for the formation of perfect 1D heterostructures. Furthermore, we elucidate the handedness correlation between the SWCNT template and BNNT crystals. This work not only provides an in-depth understanding of this 1D heterostructure material group but also, in a more general perspective, serves as an interesting investigation on crystal growth on highly curved (radius of a couple of nanometers) atomic substrates.

one-dimensional van der Waals heterostructure | carbon nanotube | transmission electron microscopy

Two-dimensional (2D) atomic layer materials including graphene, hexagonal boron nitride (BN), and transition metal dichalcogenide (TMDC) have emerged as a research focus in the past decades (1–4). They represent a new class of crystals that were believed to be unstable before, and therefore, their discoveries allowed the exploration of new physics and development of novel devices. Van der Waals (vdW) heterostructures, which are artificial stacks of these different atomic layers, further extended the research scope of 2D materials (5). These heterostructures offer a nearly unlimited freedom to combine crystals beyond conventional limits of crystal type and lattice matching (6). This generated a lot of interesting progress from fundamental crystallography and physics to optical and electronic devices (7–11). However, the concept of the vdW heterostructures has mostly been investigated in 2D materials.

Earlier, we demonstrated the experimental synthesis of one-dimensional (1D) van der Waals heterostructures (12). BN nanotubes (BNNT) and molybdenum disulfide nanotubes (MoS_2NT) were synthesized by chemical vapor deposition (CVD) on a single-walled carbon nanotube (SWCNT) template. As a result, coaxial heterostructures consisting of different nanotube crystals were generated. The growth of these heteronanotubes were shell by shell, a very different growth process from the conventional growth of 1D homo-material nanotubes in which multiple walls are formed simultaneously from a nanoparticle. Studying nucleation and crystal growth behaviors in 1D vdW heterostructures is of fundamental research interest but is challenging, as all processes occur on tiny (only a couple of nanometers) and highly curved surfaces (13, 14).

Transmission electron microscopy (TEM) is one of the most powerful tools to study the atomic arrangement of a nanomaterial. Recent advances even enabled the identification of local electronic state or even phonon state in a crystal (15, 16). However, one well-recognized obstacle is that TEM observation usually requires a complex sample preparation process. This preparation

Significance

We recently synthesized coaxially nested one-dimensional van der Waals heterostructures in which boron nitride nanotubes or molybdenum disulfide nanotubes grew seamlessly on a single-walled carbon nanotube template. In this work, edge structures, nucleation sites, and crystal epitaxial relationships in heteronanotubes are unambiguously revealed by a nondestructive transmission electron microscopic technique. These understandings, together with the characterization technique developed here, can help to optimize the synthesis process. Structure-controlled heteronanotubes may, ultimately, be used to build nanoscale devices such as gate-all-around nanotube transistors.

Author contributions: S.M. and R.X. designed research; Y.Z., A.K., K.H., K.O., G.W., Y.S., M.L., T.I., D.T., Q.Z., A.A., and R.X. performed research; E.I.K., K.S., and Y.I. contributed new reagents/analytic tools; Y.Z., A.K., K.H., K.O., S.C., D.T., E.I.K., Y.L., K.S., Y.I., S.M., and R.X. analyzed data; and Y.Z., A.K., T.I., Y.L., S.M., and R.X. wrote the paper.

The authors declare no competing interest.

This article is a PNAS Direct Submission.

This open access article is distributed under Creative Commons Attribution-NonCommercial-NoDerivatives License 4.0 (CC BY-NC-ND).

[1]Y.Z. and A.K. contributed equally to this work.

[2]Present address: Department of Materials Science and Engineering, Northwestern University, Evanston, IL 60208.

[3]To whom correspondence may be addressed. Email: xiangrong@photon.t.u-tokyo.ac.jp or maruyama@photon.t.u-tokyo.ac.jp.

This article contains supporting information online at https://www.pnas.org/lookup/suppl/doi:10.1073/pnas.2107295118/-/DCSupplemental.

Published September 10, 2021.

process not only makes TEM characterizations inefficient but also often results in a change of the material geometry or loss of intrinsic sample information. Recently, we developed an approach using a high-temperature stable Si/SiO_2 TEM grid (17). This grid is fabricated by microelectromechanical systems techniques starting from a Si/SiO_2 wafer. It can be used to support high-temperature reactions in the same way as conventional Si wafers but, at the same time, is also compatible to advanced TEM observations. This route allowed us to observe the geometry and the atomic arrangement of a nanomaterial efficiently without sample processing. Most importantly, it becomes possible to keep and reveal the original geometry, structure details, and even the evolution after high-temperature processing.

In this study, we combine this TEM approach with the growth of 1D vdW heterostructures and investigate the growth processes of BNNTs on SWCNT templates. Benefitting from the transfer-free strategy, the heterostructures were kept in their most intrinsic morphology, and many structural details can be clearly visualized. Several fundamental issues such as edge structure, nucleation behavior, and requirements for a perfect growth are then able to be unambiguously illustrated. Furthermore, we investigated the handedness correlation between grown nanotube(s) and the template, which is a unique geometric feature for 1D multilayers yet was very difficult to investigate and thus barely understood. Global and local energy difference between uni- and contrahanded heterostructures were calculated to present some theoretical insights into the experimentally observed semiepitaxial relationship.

Results and Discussion

Overview of Our TEM Approach and 1D vdW Heterostructure. Fig. 1 shows an overview of the TEM strategy we used as well as the structure of the 1D vdW heterostructures that we synthesized directly on our high-temperature-stable TEM grids. The TEM grid is made of Si and SiO_2, with a thin SiO_2 layer as support. In this study, suspended SiO_2 is also etched so that there are empty windows that can support SWCNT networks (Fig. 1*A*). Because this grid is stable up to 1,100 °C, we can use it directly in a CVD growth furnace. The grid is compatible with use in most TEM holders. At a slightly reduced beam density, various structural and elemental characterization can be performed directly on this grid without any treatment. This strategy significantly improves the efficiency of TEM to reveal the original geometry and the structure details of our heteronanotubes. With the assistance of coordinates or markers on the grid, we are able to observe the same location (*SI Appendix*, Fig. S1) and even the exact same nanotube before and after a high-temperature CVD. One example is shown in Fig. 1*B*. The original nanotube is single walled, but after a BN CVD, two to three additional layers appeared on the surface of this SWCNT. By this strategy, the growth of additional BNNTs can be straightforwardly illustrated. When putting a SWCNT–BNNT structure into another CVD process, a ternary heterostructure of SWCNT–BNNT–MoS_2NT can also be fabricated. The example in Fig. 1 *C–E* is a coaxial nanotube containing one layer of carbon, three layers of BN, and one layer of MoS_2. Different materials can be clearly visualized by the image and electron energy loss spectroscopy (EELS) mapping.

Open Edge Growth of 1D vdW Heterostructures. As heterostructures were directly synthesized on the Si/SiO_2 TEM grid, this "heterostructure on-grid" sample can be brought from our CVD chamber to the TEM column without further processing. Many intrinsic details of the heterostructure can be thereby preserved. The first thing we noticed is that the open ends of BNNTs can be visualized by TEM. Under-focused images, even by conventional high-resolution TEM (HRTEM), can reveal the shape of a tube edge, and this shape is found to be different from tube to tube. Fig. 2*A* represents three typical types of open edges we observed. These edges of BNNTs usually have sharp-cut shapes but are cut diagonally with various inclination angles from the circumference of the nanotube. For example, NT#1 has a clear spiral end, and the edge inclination angle (between the edge and tube circumference) is roughly 30°, while NT#2 has an edge nearly perpendicular to the SWCNT axis. To distinguish the difference between these two tubes, nano-area electron diffraction (NAED) was employed to determine the chiral angle (crystal orientation) of outer BNNTs (18). NAED patterns in Fig. 2*B* suggests that NT#1 is a near-armchair BNNT with the chiral angle of 28°, while NT#2 is a near-zigzag BNNT with the chiral angle of 2°. Plotting the atomic arrangement of these nanotubes in Fig. 2*C* immediately reveals that, in both cases, the sharp cuttings we observe correspond to the zigzag edge of a BN honeycomb lattice.

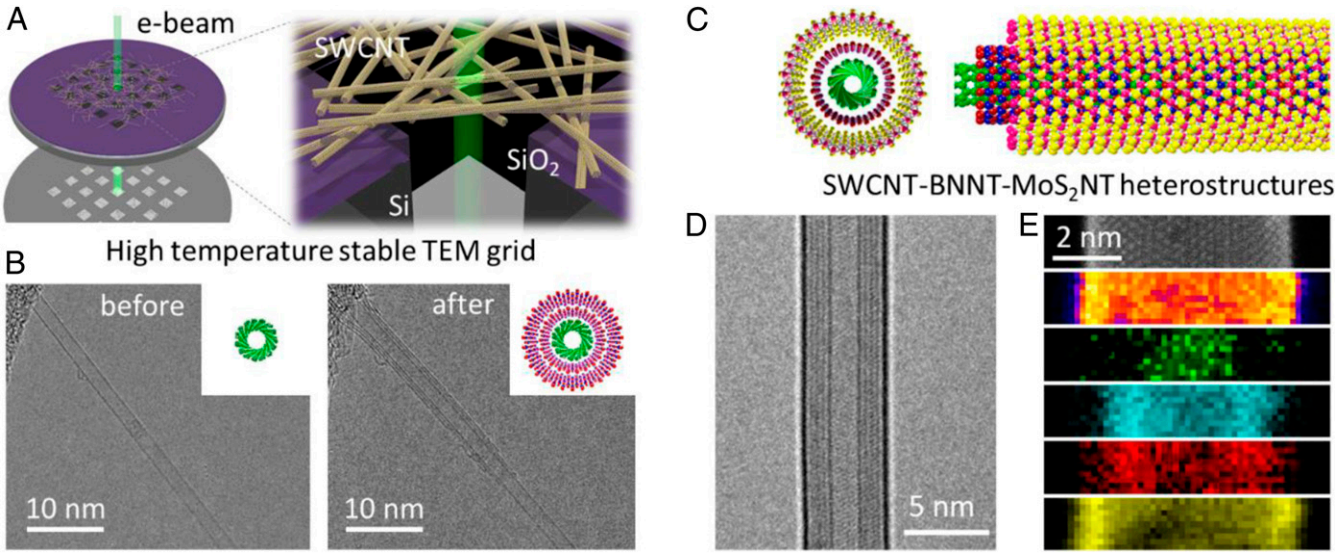

Fig. 1. The experimental strategy showing the growth of 1D vdW heterostructures directly on a TEM grid. (*A*) Schematic of the high-temperature-stable TEM grid. (*B*) TEM images of the exact same SWCNT before and after the growth of outer BNNT. (*C*) Atomic model, (*D*) TEM image, and (*E*) EELS mapping of a SWCNT–BNNT–MoS_2NT heterostructure (green, blue, red, and yellow indicate the elemental distribution of carbon, boron, nitride, and sulfur, respectively).

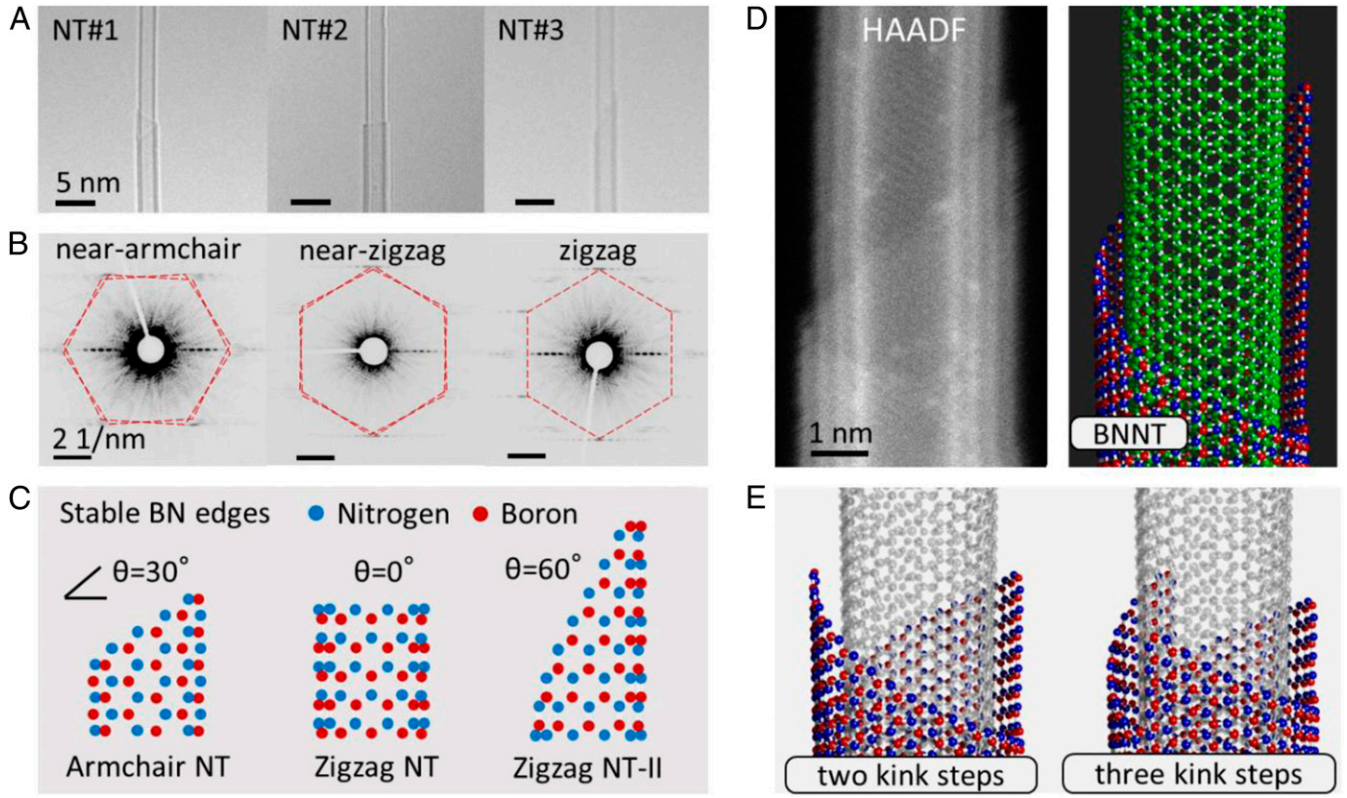

Fig. 2. Characterization of the open-growing edge of the 1D vdW heterostructure. (*A*) TEM images of three different heteronanotubes showing each outer BNNT usually has a sharp-cut open edge, but the edge is aligned to the nanotube circumference with different angles. (*B*) NAED patterns of these corresponding three nanotubes, suggesting the chiral angle of outer BNNTs are 27°, 3°, and 0°, respectively. (*C*) Expected atomic arrangements at the edge of these three BNNTs revealed by NAED patterns, indicating that the sharp-cut edges are *N*-terminated zigzag BN side. (*D*) Experimental HADDF–STEM image of a BN edge and its schematic (not exact) atomic structure. (*E*) Schematics showing open edges with two or three kink steps. In this case, the inner nanotubes are made semitransparent to show all kinks.

That is, an open-ended BNNT in this study prefers a zigzag edge over an armchair edge. This is consistent with previous theoretical and experimental studies in 2D BN in which the zigzag edge is found to be energetically more favorable (19–21). With this ability of observing the edge shape and identifying the chiral angle for the same nanotube, we learned that the open end of a BNNT is aligned to its axis with an angle depending on its own chiral index. An armchair BNNT tends to have a spiral edge (NT#1), while a zigzag BNNT has a perpendicular edge (NT#2), both of which are due to the preference of a zigzag edge. This correlation is straightforward and clearly demonstrated by the above characterizations.

However, one must take into account the difference in structural polarity when describing the edge of a BNNT (unlike a CNT in which all atoms are carbon), and this polarity explains a second type of edge shape for zigzag BNNTs shown in NT#3. Because of the crystal symmetry, a zigzag BN edge can be either terminated with B (B-polar) atoms or N atoms (*N*-polar), and studies in 2D material indicated that the *N*-terminated zigzag edge formation is energetically more stable. Therefore, when a zigzag BNNT is *N*-polar in its growing direction, a flat-cut edge is stable as shown in NT#2. However, when a zigzag BNNT is B-polar in its growing direction, a flat-cut edge becomes unstable and must grow to a 60° inclination angle to form the *N*-termination. This is exactly the case for NT#3. The chiral index of this BNNT is zigzag (34, 0), as suggested by the NAED pattern. Its chiral angle, 0°, is nearly the same as NT#2, but the edge shape is completely different. This indicates that the polarity of open ends in NT#2 and NT#3 are opposite, with NT#2 *N*-polar up and NT#3 B-polar up. Therefore, more generally, chirality of the BNNT, together with the polarity of the tube-growing direction, determines the stable edge structure of outer BNNTs. More discussions on this point, including the comparison between graphene and hexagonal BN (*SI Appendix*, Fig. S2) (22), edge structure of a chiral BNNT (*SI Appendix*, Fig. S3), and the method to extract the diffraction of BNNT from the two sets of patterns (*SI Appendix*, Fig. S4), are provided in *SI Appendix*.

Scanning TEM (STEM) was actively employed in the past decade to perform atomic-scale analysis for material science. Especially, high-angle annular dark-field (HAADF) STEM imaging is a critical tool to evidence foreign heavy atom inclusion inside materials. One representative HAADF STEM image of an open end of a BNNT is shown in Fig. 2*D*. First, this HAADF image further supports that the tube end has a zigzag edge, as a lattice space contrast of 0.21 nm appears in this image and is about 30° to the tube circumference. A second point we can elucidate from this HAADF STEM imaging is that the growth outer BNNT is a metal-free process. Although there are always small amounts of Fe remaining in the starting SWCNT network (23), it seems that no Fe atoms served as the catalyst for the extension of BNNT in the current growth scenario. This can be evidenced by STEM image simulation. If we add one Fe to any atomic position of our structure model, a very bright point contrast will appear. By comparing experimental and simulated images, we can conclude that the heteronanotubes followed a metal-free growth model. This is also supported by the very slow growth of the outer BNNTs. The growth rate is about several nanometers per minute, which is three to five orders of magnitude slower than catalytic growth of 1D or 2D BN (24, 25). In addition, in all our observations, every BN edge has only one major kink step rather than multiple zigzag kink steps (Fig. 2*E*). It is still unclear at this stage,

but the number of kink steps was expected to affect the growth dynamics of the open-growing nanotube as has been predicted by a previous theory in carbon nanotube (14). It may be interesting to study the growth dynamics for different edges in the future.

Essential Requirements for the Formation of a Perfect Heterostructure. The growth of outer BNNTs started from the nucleation on the surface of an SWCNT template, and we confirm that isolation and surface cleanness are two essential requirements for the successful formation of perfect heterostructures. The requirement for an isolation is straightforward to understand, and Fig. 3 shows two situations of BN coating when nanotubes are not well isolated. In the first case as shown in Fig. 3 *A* and *B*, a single SWCNT is laying on a quartz substrate, and cross-sectional TEM reveals that the BN coating covers the upper half of the SWCNT rather than lifting the SWCNT to generate a seamless, cylindrical structure. A gentle but distinguishable contrast difference between upper resin and lower quartz can be observed in Fig. 3*A*, and energy-dispersive X-ray spectroscopy (EDS) in Fig. 3*B* further verifies the existence of an interface, at which a SWCNT and multiple BN layers locate. In another case, if several SWCNTs are touching each other in a bundle form, BN coating covers the outer surface of the entire bundle and is unable to separate these SWCNTs and form perfect heterostructures on each SWCNTs (Fig. 3 *C* and *D*).

The second essential requirement for the formation of a heteronanotube is the surface of the template SWCNT. Perfect heterostructures can only be formed on an ultraclean SWCNT. Fig. 4 shows the different coating behaviors for BN on a clean SWCNT network and an amorphous carbon contaminated SWCNT network. All the TEM, STEM, EDS, and selected-area electron diffraction (SAED) analyses were performed under the exactly same machine condition to achieve a strict comparison. On a clean SWCNT surface, usually one or two layers of BN are formed from a single starting point, while on carbon-contaminated SWCNT surfaces, BN usually nucleates from multiple sites and grows into a multilayer, poly crystal nanotube. Over the whole area, the BN signals are much stronger on carbon-contaminated SWCNT networks than the clean ones, suggesting that intentionally deposited carbon or other unintentional contaminations may serve as nucleation sites of the outer BNNT growth. Therefore, in order to obtain perfect heteronanotubes, it is indispensable to avoid contaminations to SWCNT templates. In our process, this is achieved by using an ultraclean SWCNT. Furthermore, the use of our low-pressure CVD chamber also contributes to the formation of high-quality 1D heterostructures.

From another perspective, this finding can be used to achieve a site-selective growth of heterostructures, which may be an important step for electronic device or optical characterizations. One example is demonstrated as Fig. 4 *C*–*F*. In this experiment, we intentionally deposited some carbon using electron beam at a small local area of a clean SWCNT before putting this nanotube into the BN CVD. As expected, the growth started from the position where carbon is deposited as can be evidenced by TEM and STEM-HAADF imaging and EDS mapping.

Without intentional deposition, BNNT growth usually starts from the tube–tube contacts (shown in *SI Appendix*, Fig. S5), where BN precursors may accumulate more easily. This phenomenon is particularly clear when an individual tube-enriched SWCNT network is used as the starting growth template (26). The nucleation of BNNT from tube–tube contacts usually results in different modes, one-end nucleation or both-end nucleation on an isolated nanotube. In a both-end nucleation, two outer BNNTs can have different chiral indexes, although they are formed on the same SWCNT. They can even meet each other to form a junction when the CVD time is long enough. This is conclusively evidenced by NAED patterns or by the different wall contrast (to be further described in *Handedness*

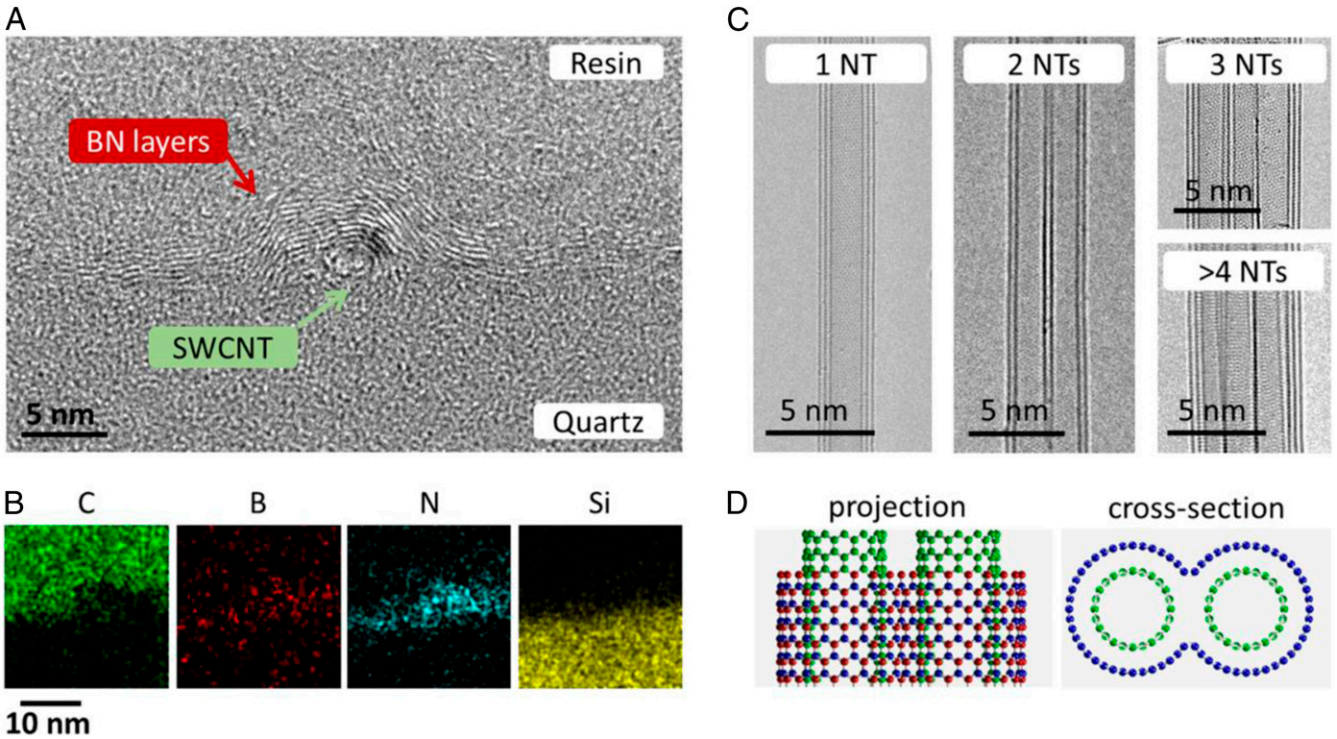

Fig. 3. Importance of isolation. (*A*) Cross-sectional TEM image and (*B*) EDS elemental mapping of BN coating on a SWCNT laying on a quartz substrate, suggesting BN covers only the top half of the SWCNT and cannot detach SWCNT from the substrate to form a seamless cylinder. (*C*) TEM images of the one- to two-layer BN coating on an individual SWCNT, a two-NT bundle, a three-NT bundle and a larger bundle, confirming BN wrap the entire bundle other than isolating the nanotubes inside a bundle. (*D*) Expected projection and cross-sectional view of the BN wrapping on a bundle.

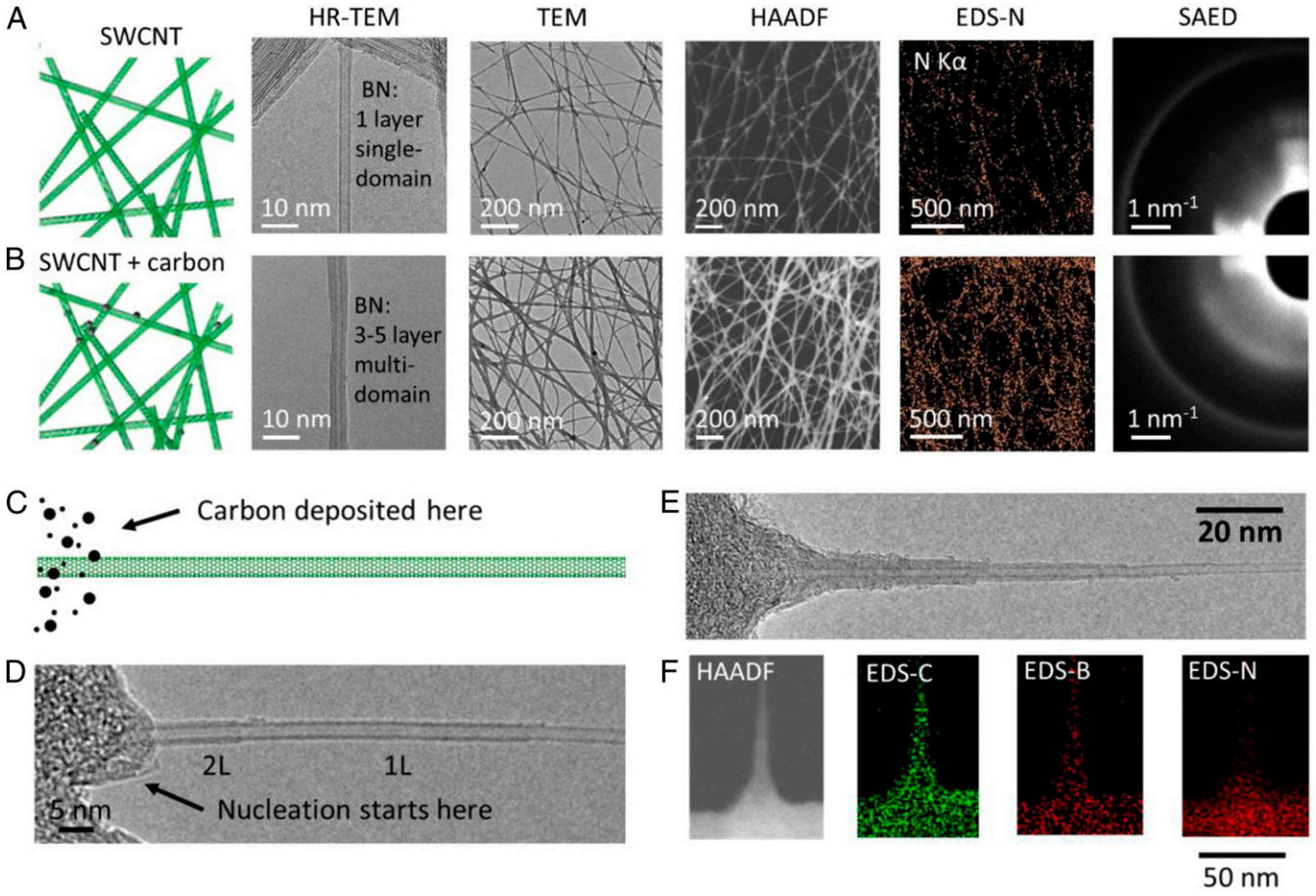

Fig. 4. Importance of cleanness. A comparison of BNNT growth behaviors on (*A*) clean SWCNT networks and (*B*) SWCNT networks with intentionally deposited amorphous carbon, suggesting that BNNT can nucleate from a single site and grow into a perfect crystal on a clean SWCNT surface, while multiple nucleation and polycrystalline growth occurs when there are contaminations on a SWCNT surface. (*C*–*F*) This strategy may be used to achieve a site-selective growth as revealed by TEM imaging and EDS mapping.

Relation in 1D vdW Heterostructures). Occasionally we also observe the growth of BNNT at the center of an isolated nanotube, but this center-nucleation mode is less predominant. The summary of these three different nucleation modes and an aberration-corrected image of a BNNT junction are provided in *SI Appendix* (*SI Appendix*, Fig. S6).

Handedness Relation in 1D vdW Heterostructures. Previously, we have confirmed that there is no obvious chirality correlation between the inner SWCNT and outer BNNT in a heterostructure (12), but the handedness correlations still remain unknown. Handedness is a unique structural feature for 1D tubular nanostructures, and the experimental identification is extremely difficult (27, 28). It is usually recognized as the ultimate structure characterization for a nanotube, as a left-handed nanotube and a right-handed nanotube have a mirror symmetry for their atomic arrangements but are supposed to have exactly the same electronic and chemical properties (Fig. 5*A*) (29). There are only a couple of techniques that have been proven capable of identifying handedness (30–33).

In TEM imaging, a right-handed (12, 6) nanotube and left-handed (6, 12) nanotube show similar contrasts. Electron diffractions, although capable of telling the chiral index of a nanotube, cannot distinguish a left-handed nanotube from a right-handed one, as their patterns are exactly the same. Despite the technical challenges, identifying the handedness is scientifically meaningful, particularly in the case of a heterostructure. One reason is that, if one would unfold a double-walled heteronanotube (should have four different combinations as shown in Fig. 5*B*), even for the same configuration, for example (17, 13)@(34, 0), a left–left handed (L@L) and left–right handed (L@R) have completely different stacking angles and thus moiré patterns. Considering the recent progress in moiré physics (e.g., in both graphene–graphene and graphene–hBN) for 2D crystals (34), and more recently 1D double-walled carbon nanotube (e.g., moiré-induced tube–tube coupling and new states) (35), it is not only important to satisfy fundamental scientific curiosity in crystallography but also of great importance to understand how the properties of a heteronanotube may be affected by their atomic arrangements.

A simple TEM technique for the identification of handedness in 1D nanotubes is to use side-wall contrast (36). In brief, when a nanotube is tilted to a certain angle in TEM, a discontinuous, dots-like contrast, which originates from a 0.21-nm zigzag atomic chain of the hexagonal honeycomb lattice, will appear at one side of projected TEM image depending on which handedness the nanotube is. Fig. 5 *C* and *D* show the scheme of this method. Historically, when this method was proposed, a nanotube needed to be tilted to its nearly exact chiral angle to see a clear side contrast. For example, a (12, 6) nanotube needs to be tilted to 19° in order to see this side-wall armchair contrast. However, with recent development of aberration-corrected TEM and hence the improvement of the point resolution, we notice that even within ±5°, side-wall contrast of a nanotube can be observed in our aberration-corrected TEM. For a (12, 6) nanotube having a chiral angle of 19°, within the range when the tube is tilted from 14 to 24°, the side-wall contrast can be distinguished. This decently large angle tolerance

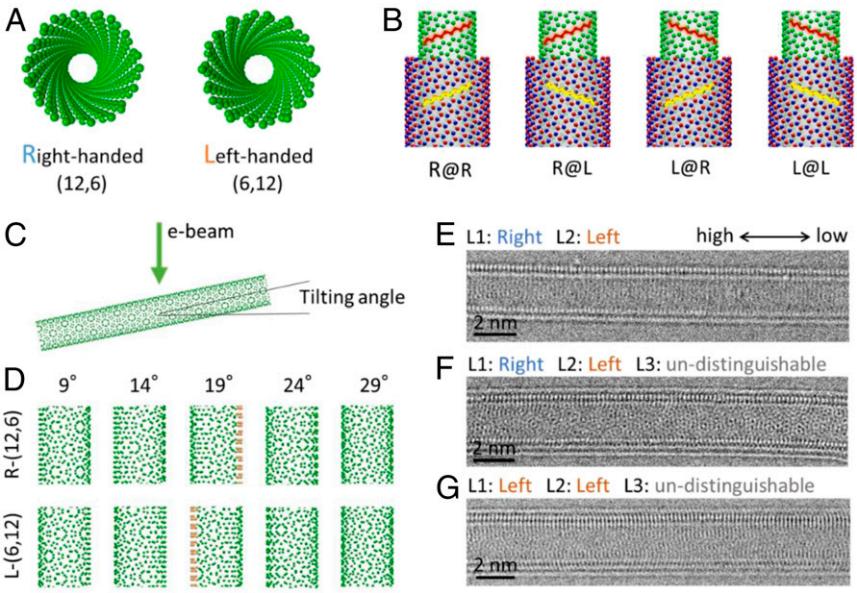

Fig. 5. Handedness relationship in 1D SWCNT–BNNT vdW heterostructures. (*A*) Geometry and definition of right-handed and left-handed nanotube. (*B*) In a double-walled SWCNT–BNNT heterostructure, four different handedness combinations, R@R, R@L, L@R, and L@L, can appear. (*C* and *D*) The experimental approach to identify the handedness of a SWCNT or BNNT nanotube in a TEM. When a nanotube is tilted, a dot-like contrast appears at one side of the wall depending on the handedness of the nanotube. (*E*–*G*) Representative TEM images of three SWCNT–BNNT heterostructures having different handedness combinations.

suggests that, in a SWCNT network where chiral indexes of SWCNTs are randomly distributed (as confirmed previously), we can roughly identify the handedness of one-third of the nanotubes among the whole population by only tilting the TEM holder to one angle. This is a convenient way to identify many nanotubes in the sample or many walls in one multiwalled heteronanotube. Occasionally, we can also observe a 0.12-nm armchair contrast at the wall (but this requires the nanotube to be titled in a very narrow angle range), which can help to further identify more nanotubes. A detailed explanation to this method, including the mechanism and examples of the side-wall contrast, are provided in *SI Appendix* (*SI Appendix*, Fig. S7).

Representative experimental data are shown in Fig. 5 *E*–*G*. In all these three images, the sample is tilted, as the left side is higher in TEM, and the right side is lower. In Fig. 5*E*, clear contrast appeared at the bottom wall for the inner tube and at the upper wall for the outer BNNT, which suggests that the inner nanotube is right-handed and the outer nanotube is left-handed. The second example in Fig. 5*F* is a triple-walled heteronanotube. The inner and middle shells also have a contrahandedness, but the outer shell is undistinguishable, as no obvious contrast appears at either side of the walls. This indicates the chiral angle of this outmost shell is beyond the range of tilting angle ±5°. The third heteronanotube, however, has a uni-handedness. Both the inner and middle shells are left-hand, while the outer shell is also undistinguishable. We listed the number 1 to 10 nanotubes we studied as Table 1, and the whole data set can be found in *SI Appendix* (*SI Appendix*, Table S1).

As a brief conclusion for all the nanotubes (meaning all distinguishable shells in all heteronanotubes we studied), we found 52 left-handers and 44 right-handers. It is reasonable that two types of nanotubes are half and half. In addition, there are also a decently large number of near-zigzag nanotubes observed. However, there are only two near-armchair nanotubes picked up by TEM. This is a limitation of TEM and does not reflect the real abundance of near-armchair nanotubes inside the whole population.

When comparing the handedness correlation for different shells within a same heteronanotube, a summary is presented in Table 2. First, between the first shell (SWCNT) and the second shell (BNNT), we found 27 sets having a uni-handedness, while 22 sets have a contrahandedness. The numbers are enough to prove that there are no obvious correlations between the SWCNT and grown BNNT. However, when counting the second shells and beyond, a weak tendency of having the same handedness begin to appear. To be specific, among the 51 sets of data we obtained, 37 pairs are uni-handed.

To understand the mechanism behind these TEM-obtained results, we performed a theoretical calculation with empirical potentials on the different combinations of SWCNT and BNNTs. We started from a uni-handed and a contrahanded double-walled BNNT. Fig. 6*A* illustrates the atomic energy distribution of these two structures. Details of the calculated energy values are available at *SI Appendix*, Tables S2 and S3. The first thing we learned is that the global energy difference between a uni-handed and a contrahanded heterostructure is negligible. Although atomic configuration and therefore local energy are apparently different place by place (as revealed in Fig. 6 *B* and *C*), the whole nanotube is, to our surprise, energetically averaged, causing the absence of any structural preference (unfolded view in *SI Appendix*, Fig. S8). This indicates that the experimentally observed tendency of having a uni-handedness in the second layer and beyond is not because the uni-handedness is energetically more stable in equilibrium. However, the growth of heteronanotubes is a dynamic process, and it usually started from nucleating a small site on the surface of an existing nanotube. Therefore, these locally formed small sites/fakes, if having any energy preference, will determine the chirality and handedness of the resulting material before a seamless circumference is formed.

To deliver this concept of "local preference," we plotted the average cohesive energy of a triangle flake versus its flake length (L = number of hexagons at each side of the triangular flake) for contrahandedness and uni-handedness in Fig. 6 *D* and *E*. When the flake is placed randomly on the surface of SWCNT, the energy varies with the position, which causes an energy distribution in the *y*-axis. By this approach, the local energy difference can be clearly visualized—the local energy distribution is broader in a

Table 1. Summary of the handedness information in all nanotube shells

No. of NT	1	2	3	4	5	6	7	8	9	10
First layer (C)	R*	R	L	R	Z	Z	Z	Z	R	Z
Second layer (BN)	L	L	L	R	L	L	R	Z	R	L
Third layer (BN)		?	?	R	L		R	Z	?	L
Fourth layer (BN)				R	L			L		
Summary	Left-handed		Right-handed		Near-zigzag		Near-armchair			
Counts	52		44		58		2 (TEM-limited)			

*R, right-handed; L, left-handed; Z, near-zigzag; ?, undistinguishable.

uni-handedness (Fig. 6*E*) than a contrahandedness combination, but exact values at some locations are smaller, meaning these locations are energetically more favorable. Small flakes may prefer to nucleate at these "comfortable locations" to form uni-handed seeds, which finally further grow into a uni-handed nanotube. In short, although there are more "uncomfortable" locations in a uni-handed case, there are also more "very comfortable locations" for nucleation, particularly at the early stage when the flake is small.

This local preference is more significant beyond the second layer probably because of two possible factors. The first factor is the material effect. Materials starting from layer two are homogenously BN and therefore may prefer uni-handedness or even similar chiral angles. This material effect could be smaller between SWCNT and BNNT. The second and more likely factor is the diameter effect. When one additional layer forms on a nanotube, the diameter increases about 0.7 nm. For larger diameter nanotubes, the outer surface is less curved. Local preference on a less-curved surface will be more likely to be more significant, behaving more similarly to local epitaxial nucleation to a flat 2D surface.

We performed the same calculations on a double-walled CNT–BNNT heterostructure and a smaller diameter BNNT–BNNT homostructure and extracted their conformable energy spots ($E_{\min}$ value). The difference between uni-handness and contrahandedness ($E_{\min,\mathrm{uni}} - E_{\min,\mathrm{contra}}$) is plotted in Fig. 6*F* and compared with the previous double-walled BNNT–BNNT. Although it is still hard to quantify the material effect and curvature effect for a large number of different pairs, and in a more collective way, material effects are clearly observed (blue line versus black line in Fig. 6*F*). Therefore, the combinational effect of these two factors is expected to determine the extent of interwall epitaxy and explains the tendency of handedness correlation observed in our TEM characterizations. However, the diameter effect may be more determinative. Ultimately when the curvature disappears, 2D BN flakes are usually grown epitaxially following the orientation of a graphene substrate (24). Despite that further efforts are still needed to fully understand this tendency, the random correlation on the first shell, and the later preference of uni-handedness on second layer and beyond, seem to be convincing and conclusive in the study. This may help us to understand the shell–shell interaction and thereby how the optical, electronic, topological, and other properties of a hetero-nanotube may be modulated (37–42). Possibly, it will also be beneficial for the design of different and new heterostructures for devices (13, 43, 44).

Conclusion

In summary, we have performed a systematic study on the growth mechanism and the crystal epitaxial correlation in 1D vdW heterostructures. As benefited from the CVD-compatible TEM approach, the original geometry and intrinsic structural details of the heterostructures are preserved and become conveniently accessible. The key findings are summarized as follows: 1) 1D SWCNT–BNNT vdW heterostructures follow an open-end growth model, and the end of an outer BNNT has a sharp-cut edge, which is aligned to the tube circumference at an angle depending on its own chiral index and polarity. The mechanism behind this phenomenon is that BNNT open edges always prefer *N*-zigzag termination as was evidenced by NAED patterns and direct TEM/STEM imaging. 2) Having a well-isolated, ultraclean SWCNT is essential to obtain a perfect heterostructure, as BN will cover the only half of the tube or over the entire bundle if the tube is attaching to a substrate or other nanotubes. Furthermore, cleanness of the surface is also essential to start a single site nucleation and form a single crystal domain on the nanotube. However, intentionally introduced nucleation sites may be utilized to achieve a site-selective fabrication of heterostructures. The nanotubes usually nucleate from the tube–tube contacts, and this resulted in three different growth cases: one-end growth, two-end growth, and center growth. 3) The cutting-edge aberration-corrected TEM allowed to identify the handedness of roughly one-third of the nanotubes among the whole population. The handedness of the inner and outer nanotubes was confirmed to be random, but there was a gentle tendency toward the same handedness beyond the third layer. This was not because of an energetic preference between different handedness combinations, as the global energy difference between uni- and contrahandedness is very small but probably caused by the local structure preference, which happened at the nucleation stage on the surface of the templated nanotube. These effects are expected to be more significant for homo-materials and larger diameter nanotubes.

These comprehensive results were obtained on Si/SiO_2-based TEM grids, which can serve as a very effective route from CVD to TEM to study the atomic structure of an as-grown nanomaterial and to understand its formation behaviors. This TEM approach itself is robust and universal and may be used for other material synthesis or other catalytic processes. The knowledge we learned on the growth mechanism and crystal relationship may be beneficial to understand the properties, especially the tube–tube interaction of our current SWCNT–BNNT–MoS_2NT heterostructures, and may be helpful for the controlled synthesis

Table 2. Summary of the correlation between inner and outer nanotubes

First interlayer (SWCNT–BNNT)		Second interlayer and beyond (BNNT–BNNT)	
Same	Different	Same	Different
27	22	37	14
55.1%	44.9%	72.5%	27.5%

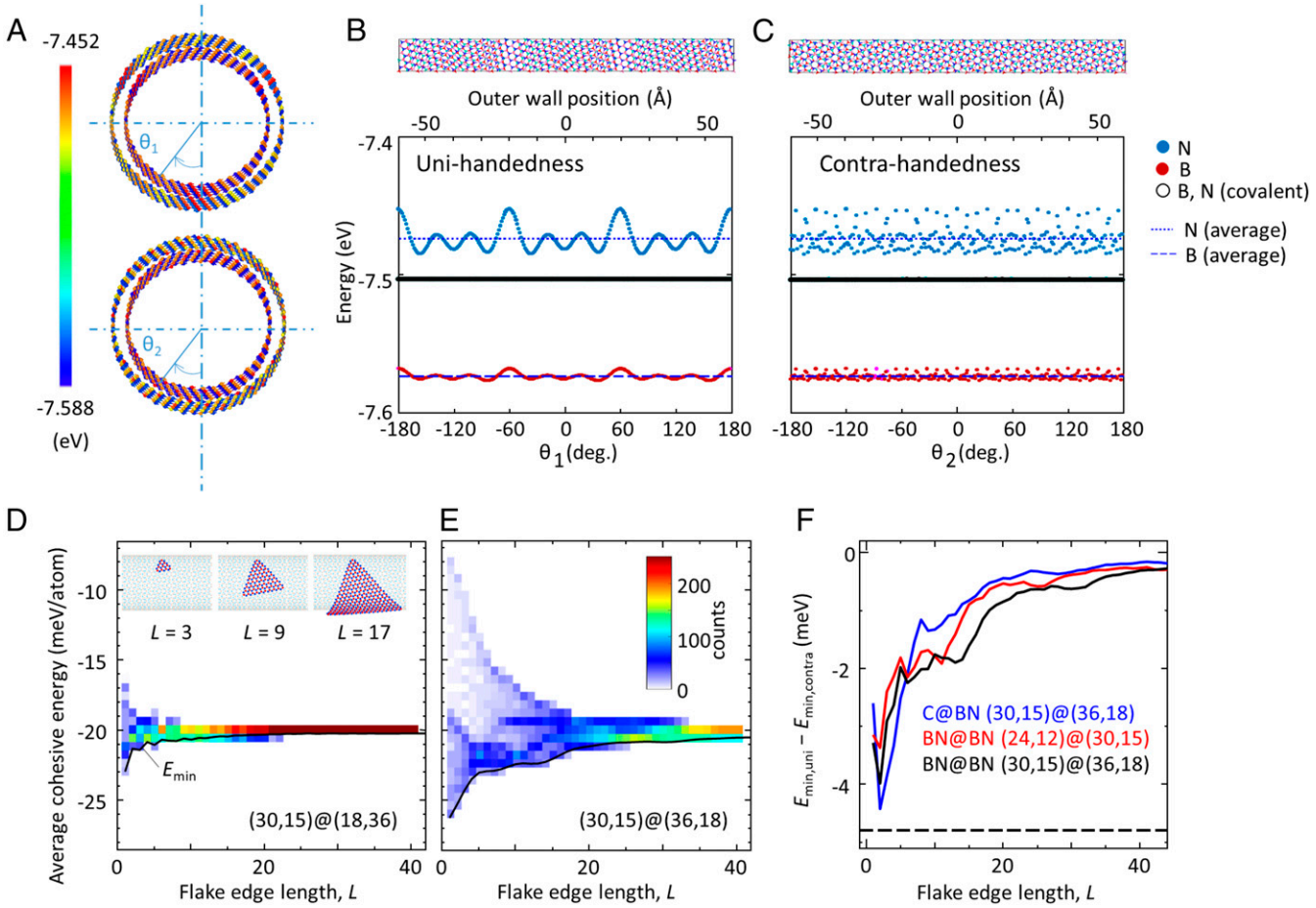

Fig. 6. Simulated global and local energy difference in uni- and contrahanded heterostructures. (*A*) A color map of interatomic potentials of each atom, where θ_1 denotes the circumferential position for DW-BNNT (30, 15)@(36, 18), and θ_2 denotes the position for (30, 15)@(18, 36). (*B*) Interatomic potential of each atom as a function of the circumferential position θ_1. (*C*) Interatomic potential of each atom as a function of the circumferential position θ_2. Magenta, cyan, and black points in *B* and *C* denote potential energy of N, B, and both with only covalent bonds, respectively. Blue dashed and dotted lines denote averaged potential energy per atom for B and N atoms, respectively. Histograms for the cohesive energy of a triangular BN flake with various edge lengths *L* in a (30, 15)@(36, 18) (*D*) and a (30, 15)@(18, 36) (*E*) BNNT. In total, 252 positions are considered as a flake vertex, which correspond to all B atoms in a unit cell. The energy of each flake is averaged for all B and N atoms that compose the flake. Black lines represent the minimum cohesive energy E_{min} among the 252 positions considered. (*F*) Difference in E_{min} versus *L* for uni- and contrahandedness. Horizontal dashed line represents the difference of the cohesive energy in the case of AA′ (orthorhombic) stacked bilayer BN and 19.1° twisted bilayer BN. When the diameter of template NTs is infinitely large, the solid lines in *F* should be close to the dashed line until some flake size.

or even the design of new and more sophisticated 1D vdW heterostructures.

Materials and Methods

The template SWCNT film used in this project was synthesized by aerosol CVD (23). Typically, ferrocene was used as the catalyst precursor, and CO was used as the carbon source. The growth temperature was 1,000 to 1,200 °C. The SWCNTs were formed in gas phase and collected onto a filter paper.

The highly individual SWCNTs are prepared in an injection-floating catalytic CVD (26). A total of 8,000 standard cm^3 per minute (sccm) of H_2 carrier gas and 11 sccm of C_2H_4 carbon source were introduced, and 4.0 $\mu L \cdot min^{-1}$ of mixed solution [toluene (10 g), ferrocene (0.3 g), and thiophene (0.045 g), acting as a carbon source, catalyst precursor, and growth promoter, respectively] was injected into the reactor by a syringe pump. The growth temperature was set to be 1,100 °C.

Horizontally aligned SWCNTs were synthesized on crystal quartz substrates by alcohol catalytic CVD (45, 46). Fe (nominal thickness of 0.2 nm) was prepared by thermal evaporation and patterned into line shape with 300-μm spacing by e-beam lithography. Typical SWCNT growth was performed at 800 °C and with an ethanol pressure of 140 to 150 Pa.

SWCNT–BNNT heterostructures were synthesized by a low-pressure thermal CVD using ammonia borane (H_3NBH_3) as the BN precursor (12). Briefly, the starting SWCNT prepared in the previous section was placed at the center of the furnace. A total of 30 mg BN precursor was loaded at the upstream and heated to 70 to 90 °C. The vapor of BN precursor was taken by a flow of 300 sccm Ar (with 3% H_2) to the hot zone to form BNNT on the surface of SWCNTs. The reaction temperature was 1,000 to 1,100 °C, and the chamber pressure was maintained at 300 Pa. The coating time in this study varied from a few min to 1 h.

SWCNT–BNNT–MoS_2NT heterostructures were synthesized by a low-pressure CVD using MoO_3 and S powder as precursors (12). S powder was placed at the upper stream and heated to 100 to 130 °C, and MoO_3 is placed at next to S and heated to 500 to 600 °C. The vapor was carried in by a flow of 50 sccm Ar to SWCNTs or SWCNT–BNNT heterostructures at the center. The temperature was maintained at 400 to 600 °C, and typical growth time varied from 5 to 70 min.

The Si TEM grid used in this study was prepared by dry etching. Briefly, a Si/SiO_2 wafer (thickness of Si 200 μm, thickness of SiO_2 600 nm for both sides) was used as the starting substrate. Photoresist patterns were prepared on the topside of the substrate by photolithography to define window structures and outer shapes of TEM grids. SiO_2 and Si were etched from the topside by isotropic-reactive ion etching to the depth of ∼20 μm. Then, the backside of the substrate was photolithographycally patterned with the similar structure as the topside but with a little larger windows followed by being etched by deep-reactive ion etching. Etching time and cycles were adjusted to completely etch through the Si and SiO_2 so that empty windows are formed for TEM observations.

Conventional HRTEM images were taken by a JEM-2800 at an acceleration voltage of 100 kV. EDS and SAED patterns of the entire film were taken by the same TEMs with a typical selected area aperture diameter of a few micrometers and a camera length of 60 cm. NAED patterns of individual SWCNT–BNNT heterostructure were obtained by JEM-ARM200F STEM with a cold field emission gun operating at 80 kV. In this case, a near parallel beam is used together with a small convergence lens aperture (10 μm in diameter) to obtain a small-area electron beam size (~10 nm in diameter). Additionally, the samples were heated at 300 °C during the measurement to avoid carbon contamination using a heating holder (EM-31670SHTH) and a controller unit (EM-08170HCU). HAADF– and ABF–STEM images and corresponding EELS mapping of SWCNT–BNNT–MoS_2 heterostructures were obtained in the same TEM or GRAND-ARM STEM operating at 80 kV. Aberration-corrected TEM images are taken at a different JEM-ARM200F TEM with a cold field emission gun operating at 120 or 60 kV.

To describe intralayer covalent bonds, a set of Tersoff potential for B, N, and C materials is applied (47), and to express interlayer interaction, a registry-dependent interlayer potential and screened Coulomb potential is used (48–50). We used the molecular dynamics package LAMMPS as an implementation of this calculation (51).

For double-walled (DW)-BNNTs, (2*n*,*n*) BNNT@(2*n*+6,*n*+3) BNNT and (2*n*,*n*) BNNT@ (*n*+3,2*n*+6) BNNT are calculated, and for CNT@BNNTs, (2*n*,*n*) CNT@(2*n*+6,*n*+3) BNNT and (2*n*,*n*) CNT@ (*n*+3,2*n*+6) BNNT are calculated as the example of uni-handedness and contrahandedness, respectively. The structure optimization is carried out under axial pressure at 1 atm for an isolated DW-NT.

Data Availability. All study data are included in the article and/or *SI Appendix*.

ACKNOWLEDGMENTS. We acknowledge Peng-Xiang Hou, Chang Liu, and Hui-Ming Cheng for providing the highly isolated SWCNT films and Hiroyuki Oshikawa for the assistance of TEM sample preparation and observation. Part of this work was supported by Japanese Society for the Promotion of Science Grants-in-Aid for Scientific Research (KAKENHI) (Grants JP18H05329, JP19H02543, JP20H00220, JP20K14660, and JP20KK0114) by Japan Science and Technology, the Core Research for Evolutional Science and Technology (CREST) Grant JPMJCR20B5, Japan, Ministry of Science and Technology (MoST) Grant 2016YFA0201904, China, National Natural Science Foundation of China (NSFC) Grant 22120102004, and by the Academy of Finland Project316572. A.K. acknowledges support from the Leading Initiative for Excellent Young Researchers of Japan Society for the Promotion of Science conducted by JEOL Ltd. G.W. was supported by Nakatani Research and International Experience for Students Fellowship Program. Part of the work was conducted at the Advanced Characterization Nanotechnology Platform of the University of Tokyo supported by the "Nanotechnology Platform" of the Ministry of Education, Culture, Sports, Science and Technology, Japan, Grant JPMXP09A20UT0063 and JPMXP09A21UT0050.

1. A. K. Geim, K. S. Novoselov, The rise of graphene. *Nat. Mater.* **6**, 183–191 (2007).
2. K. F. Mak, C. Lee, J. Hone, J. Shan, T. F. Heinz, Atomically thin MoS_2: A new direct-gap semiconductor. *Phys. Rev. Lett.* **105**, 136805 (2010).
3. J. Zhou *et al*., A library of atomically thin metal chalcogenides. *Nature* **556**, 355–359 (2018).
4. K. S. Novoselov *et al*., Two-dimensional atomic crystals. *Proc. Natl. Acad. Sci. U.S.A.* **102**, 10451–10453 (2005).
5. A. K. Geim, I. V. Grigorieva, Van der Waals heterostructures. *Nature* **499**, 419–425 (2013).
6. A. Koma, Vanderwaals epitaxy—A new epitaxial-growth method for a highly lattice-mismatched system. *Thin Solid Films* **216**, 72–76 (1992).
7. X. Hong *et al*., Ultrafast charge transfer in atomically thin MoS_2/WS_2 heterostructures. *Nat. Nanotechnol.* **9**, 682–686 (2014).
8. C. H. Lee *et al*., Atomically thin p-n junctions with van der Waals heterointerfaces. *Nat. Nanotechnol.* **9**, 676–681 (2014).
9. H. Fang *et al*., Strong interlayer coupling in van der Waals heterostructures built from single-layer chalcogenides. *Proc. Natl. Acad. Sci. U.S.A.* **111**, 6198–6202 (2014).
10. Y. Liu *et al*., Van der Waals heterostructures and devices. *Nat. Rev. Mater.* **1**, 16042 (2016).
11. K. S. Novoselov, A. Mishchenko, A. Carvalho, A. H. Castro Neto, 2D materials and van der Waals heterostructures. *Science* **353**, aac9439 (2016).
12. R. Xiang *et al*., One-dimensional van der Waals heterostructures. *Science* **367**, 537–542 (2020).
13. R. Xiang, S. Maruyama, Heteronanotubes: Challenges and opportunities. *Small Sci.* **1**, 2000039 (2021).
14. F. Ding, A. R. Harutyunyan, B. I. Yakobson, Dislocation theory of chirality-controlled nanotube growth. *Proc. Natl. Acad. Sci. U.S.A.* **106**, 2506–2509 (2009).
15. J. A. Hachtel *et al*., Identification of site-specific isotopic labels by vibrational spectroscopy in the electron microscope. *Science* **363**, 525–528 (2019).
16. R. Senga *et al*., Position and momentum mapping of vibrations in graphene nanostructures. *Nature* **573**, 247–250 (2019).
17. H. An *et al*., Atomic-scale structural identification and evolution of Co-W-C ternary SWCNT catalytic nanoparticles: High-resolution STEM imaging on SiO_2. *Sci. Adv.* **5**, eaat9459 (2019).
18. J. M. Zuo *et al*., Coherent nano-area electron diffraction. *Microsc. Res. Tech.* **64**, 347–355 (2004).
19. M. Maruyama, S. Okada, Energetics and electronic structure of triangular hexagonal boron nitride nanoflakes. *Sci. Rep.* **8**, 16657 (2018).
20. Y. Liu, S. Bhowmick, B. I. Yakobson, BN white graphene with "colorful" edges: The energies and morphology. *Nano Lett.* **11**, 3113–3116 (2011).
21. Z. Zhang, Y. Liu, Y. Yang, B. I. Yakobson, Growth mechanism and morphology of hexagonal boron nitride. *Nano Lett.* **16**, 1398–1403 (2016).
22. V. I. Artyukhov, Y. Liu, B. I. Yakobson, Equilibrium at the edge and atomistic mechanisms of graphene growth. *Proc. Natl. Acad. Sci. U.S.A.* **109**, 15136–15140 (2012).
23. A. G. Nasibulin *et al*., Multifunctional free-standing single-walled carbon nanotube films. *ACS Nano* **5**, 3214–3221 (2011).
24. H. Arai, T. Inoue, R. Xiang, S. Maruyama, S. Chiashi, Non-catalytic heteroepitaxial growth of aligned, large-sized hexagonal boron nitride single-crystals on graphite. *Nanoscale* **12**, 10399–10406 (2020).
25. R. Zhang *et al*., Growth of half-meter long carbon nanotubes based on Schulz-Flory distribution. *ACS Nano* **7**, 6156–6161 (2013).
26. S. Jiang *et al*., Ultrahigh-performance transparent conductive films of carbon-welded isolated single-wall carbon nanotubes. *Sci. Adv.* **4**, eaap9264 (2018).
27. R. Saito, M. Fujita, G. Dresselhaus, M. S. Dresselhaus, Electronic-structure of chiral graphene tubules. *Appl. Phys. Lett.* **60**, 2204–2206 (1992).
28. G. G. Samsonidze *et al*., Interband optical transitions in left- and right-handed single-wall carbon nanotubes. *Phys. Rev. B Condens. Matter Mater. Phys.* **69**, 205402 (2004).
29. J. W. G. Wildoer, L. C. Venema, A. G. Rinzler, R. E. Smalley, C. Dekker, Electronic structure of atomically resolved carbon nanotubes. *Nature* **391**, 59–62 (1998).
30. G. Ao, J. K. Streit, J. A. Fagan, M. Zheng, Differentiating left- and right-handed carbon nanotubes by DNA. *J. Am. Chem. Soc.* **138**, 16677–16685 (2016).
31. Y. Chen *et al*., Helicity-dependent single-walled carbon nanotube alignment on graphite for helical angle and handedness recognition. *Nat. Commun.* **4**, 2205 (2013).
32. G. Liu *et al*., Simultaneous discrimination of diameter, handedness, and metallicity of single-walled carbon nanotubes with chiral diporphyrin nanocalipers. *J. Am. Chem. Soc.* **135**, 4805–4814 (2013).
33. X. Peng *et al*., Optically active single-walled carbon nanotubes. *Nat. Nanotechnol.* **2**, 361–365 (2007).
34. M. Yankowitz *et al*., Emergence of superlattice Dirac points in graphene on hexagonal boron nitride. *Nat. Phys.* **8**, 382–386 (2012).
35. S. Zhao *et al*., Observation of drastic electronic-structure change in a one-dimensional Moiré superlattice. *Phys. Rev. Lett.* **124**, 106101 (2020).
36. Z. Liu *et al*., Determination of optical isomers for left-handed or right-handed chiral double-wall carbon nanotubes. *Phys. Rev. Lett.* **95**, 187406 (2005).
37. M. G. Burdanova *et al*., Ultrafast optoelectronic processes in 1D radial van der waals heterostructures: Carbon, boron nitride, and MoS_2 nanotubes with coexisting excitons and highly mobile charges. *Nano Lett.* **20**, 3560–3567 (2020).
38. P. Wang *et al*., Enhanced in-plane thermal conductance of thin films composed of coaxially combined single-walled carbon nanotubes and boron nitride nanotubes. *ACS Nano* **14**, 4298–4305 (2020).
39. C. Hu, V. Michaud-Rioux, W. Yao, H. Guo, Theoretical design of topological heteronanotubes. *Nano Lett.* **19**, 4146–4150 (2019).
40. M. Liu *et al*., Photoluminescence from single-walled MoS_2 nanotubes coaxially grown on boron nitride nanotubes. *ACS Nano* **15**, 8418–8426 (2021).
41. C. Liu *et al*., One-dimensional van der Waals heterostructures as efficient metal-free oxygen electrocatalysts. *ACS Nano* **15**, 3309–3319 (2021).
42. P. H. Ying, J. Zhang, Y. Du, Z. Zhong, Effects of coating layers on the thermal transport in carbon nanotubes-based van der Waals heterostructures. *Carbon* **176**, 446–457 (2021).
43. Y. Feng *et al*., One-Dimensional van der Waals heterojunction diode. *ACS Nano* **15**, 5600–5609 (2021).
44. Y. Gogotsi, B. I. Yakobson, Nested hybrid nanotubes. *Science* **367**, 506–507 (2020).
45. S. Maruyama, R. Kojima, Y. Miyauchi, S. Chiashi, M. Kohno, Low-temperature synthesis of high-purity single-walled carbon nanotubes from alcohol. *Chem. Phys. Lett.* **360**, 229–234 (2002).
46. T. Inoue *et al*., Effect of gas pressure on the density of horizontally aligned single-walled carbon nanotubes grown on quartz substrates. *J. Phys. Chem. C* **117**, 11804–11810 (2013).
47. A. Kinaci, J. B. Haskins, C. Sevik, T. Cagin, Thermal conductivity of BN-C nanostructures. *Phys. Rev. B Condens. Matter Mater. Phys.* **86**, 115410 (2012).
48. T. Maaravi, I. Leven, I. Azuri, L. Kronik, O. Hod, Interlayer potential for homogeneous graphene and hexagonal boron nitride systems: Reparametrization for many-body dispersion effects. *J. Phys. Chem. C* **121**, 22826–22835 (2017).
49. W. Ouyang, D. Mandelli, M. Urbakh, O. Hod, Nanoserpents: Graphene nanoribbon motion on two-dimensional hexagonal materials. *Nano Lett.* **18**, 6009–6016 (2018).
50. W. Ouyang *et al*., Mechanical and tribological properties of layered materials under high pressure: Assessing the importance of many-body dispersion effects. *J. Chem. Theory Comput.* **16**, 666–676 (2020).
51. S. Plimpton, Fast parallel algorithms for short-range molecular-dynamics. *J. Comput. Phys.* **117**, 1–19 (1995).